Petroleum Science 18 (2021) 1829–1839

Contents lists available at ScienceDirect

Petroleum Science

journal homepage: www.keaipublishing.com/en/journals/petroleum-science

Original Paper

Structural optimization strategy of pipe isolation tool by dynamic plugging process analysis

Ting-Ting Wu, Hong Zhao*, Bo-Xuan Gao, Fan-Bo Meng

College of Mechanical and Transportation Engineering, China University of Petroleum, Beijing, 102249, China

ARTICLE INFO

Article history:
Received 7 May 2020
Accepted 16 December 2020
Available online 14 October 2021

Edited by Xiu-Qiu Peng

Keywords:
Pipe isolation tool
Dynamic analysis
Drag coefficient
Pressure coefficient
Modified particle swarm optimization algorithm

ABSTRACT

During the pipeline plugging process, both the pipeline and the pipe isolation tool (PIT) will be greatly damaged, due to the violent vibration of the flow field. In this study, it was proposed for the first time to reduce the vibration of the flow field during the plugging process by optimizing the surface structure of the PIT. Firstly, the central composite design (CCD) was used to obtain the optimization schemes, and the drag coefficient and pressure coefficient were proposed to evaluate the degree of flow field changes. Secondly, a series of computational fluid dynamics (CFD) simulations were performed to obtain the drag coefficient and pressure coefficient during dynamic plugging. And the mathematical model of drag coefficient and pressure coefficient with the surface structure of the PIT were established respectively. Then, a modified particle swarm optimization (PSO) was applied to predict the optimal value of the surface structure of the PIT. Finally, an experimental rig was built to verify the effectiveness of the optimization. The results showed that the improved method could reduce the flow field vibration by 49.56%. This study provides a reference for the design of the PIT surface structure for flow field vibration technology.

1. Introduction

Pipeline transportation is considered an effective method to transport different types of fluids, including oil and gas. However, because of the long usage time in service, pipelines do not operate effectively because of corrosion, wax, debris, etc. The PIT is one of the effective ways to solve these problems; this tool is remotely controlled and is operated in a pipeline isolation system in oil and gas pipelines with all the dimensions. This tool is applied to plug the high pressure inside the pipelines and the risers; therefore, it permits pipeline maintenance and repair without losing the pipeline contents and without depressurizing the pipeline. However, in the plugging process, it will cause severe vibration of the flow field. The vibration of the flow field causes serious damage to the pipeline and the PIT, thereby affecting the safety and durability of the plugging operation.

A considerable amount of research has been conducted on pipe isolation techniques over the past few years, and major advances have been in the field of mechanical design. Tveit and Aleksandersen (2000) introduced the PSI Smart Plug to plug a pipeline. The PSI Smart Plug has been successfully applied to five-dimensional bend pipes (Lie and Muangsuankwan, 2015). Although many experimental and theoretical attempts to explore the plugging process and the PIT in a pipeline, researchers have been unsuccessful in simulating this process because of the complexity of both the transport and the turbulence phenomena as well as the lack of experimental data. Therefore, a dynamic analysis of the PIT can estimate these important parameters for the designers.

There are many reasons that affect the performance of the PIT, such as the plugging material, operating velocity and the structure of the PIT. A two-dimensional axisymmetric nonlinear finite element model was proposed to predict the contact force by a bi-directional PIG (Zhu and Zhang et al., 2015). The model showed that the thickness of the sealing disc had the greatest effect on the contact force of the bi-directional PIG, followed by the chamfer dimension, then the clamping rate, and finally the interference. A brake unit with the active control of the PIG speed was developed by Liang et al. (2017) to avoid the uncomfortably high speed of PIG. Mirshamsi and Rafeeyan (2015) reported a dynamic analysis and the simulations of long PIG through the 2D gas pipelines. In the

* Corresponding author.
E-mail address: hzhao@cup.edu.cn (H. Zhao).

https://doi.org/10.1016/j.petsci.2021.09.010

modeling, the length of PIG was recorded, and the influence of the length on the plugging process was analyzed. There are few studies on other factors that affect plugging and no studies have shown the interaction between different factors. Therefore, this paper adopts the method based on response surface methodology (RSM) to study the significant relationship between various factors and the plugging vibration. The order of influence of each factor on plugging vibration is obtained by comparison.

In our previous research (Zhao and Hu, 2017), the relationship between the PIT length and the pipe diameter was demonstrated and the model of the PIT length and the force on the outer surface of the PIT was obtained. It proves that the PIT structure does have a great influence on the plugging process. However, the relationship between the structure of the PIT and the flow field vibration has not been studied. Therefore, the damage to the pipeline caused by the plugging process cannot be shown. Secondly, because previous research used static finite element analysis, it could not fully understand the impact on the PIT during the entire plugging process.

Therefore, the main objective of this paper was to optimize the structure of the PIT through dynamic finite element analysis and experiments to reduce the vibration of the flow field. First of all, the research object of this article was the external structure of the PIT, so the complex internal structure of the PIT was simplified. A PIT model that can be dynamically simulated and tested was designed. The application of RSM to design the experimental program can not only improve the efficiency of the experiment, but also verify the interaction relationship between the various parameters. A series of CFD simulations were performed on various PIT models based on natural gas pipelines. On the basis of four quantitative parameters, the mathematical model of flow field vibration and PIT structure was established. And analyzed the interaction relationship between various parameters. By building a visual experiment rig, verify the influence of different PIT structures on the vibration of the flow field during the plugging process.

2. Simplified dynamic PIT model

Vibrations appeared between the pipe and the PIT when the PIT was run inside the pipe, which affected the safety of the plugging operation (Zhang et al., 2015). The traditional plug models are made up of a pressure head, a spring guide, housing, a packer, a bowl, slips, a wheel assembly, a hydraulic cylinder, ball joint housing, a hydraulic piston, and an actuator flange (Dolejal and Tveit, 2001; Edd Tveit, 2000), which can plug pipes of different sizes. However, because of the complicated internal structure of these models, it is not convenient to study the influence of an external flow field during the plugging process. Therefore, a simplified plugging model was designed to study the optimal design for the main parameters of PIT to reduce the unsteady flow conditions. The simplified model basically restores the external form of the traditional model and the traditional size is reduced to facilitate the experimental study based on the geometrical similarity principle.

The simplified PIT model consists of an actuator, four slips, a pressure head and a bowl as shown in Fig. 1. When the PIT reached the plugging zone, the actuator pushed the slips along the slide of the pressure head until it came into contact with the left side of the pressure head to achieve self-locking. At this moment, the method of interference fit was used between the bowl and the pipe wall. When the plugging operation was completed, the actuator released pressure, and the slips moved to the left along the slide under the compression of the bowl until the bowl returned to its original state. The PIT moved towards the downstream region under the pressure difference until it was removed. The plugging operation was completed. The simplified PIT model was developed on the basis of data obtained from previous research (Zhao et al., 2016). According to the relevant parameters of the experimental rig and the Reynolds similarity principle, the initial longitudinal velocity (u) was 0.1 mm/s, the other parameter values are presented in Table 1. Based on the simplified PIT model, there were three main regions during a plugging operation: downstream zone, plugging zone, and upstream zone, as shown in Fig. 1. The upstream zone was the area from the inlet of the pipe to the end of the PIT, which was a very low liquid-hold up region. The plugging zone was the area from the actuator pushing the slips (stage 1) through the bowl interference to come into contact with the pipe (stage 2) until the bowl was restored to its original state. The downstream zone was the area from the location of the PIT to the end of the pipeline that PIT had not affected until then.

3. Optimal experimental design schemes

A number of investigations have been carried out both experimentally and theoretically on the pressure and the velocity distribution in a pipe during the plugging process (Solghar and Davoudian, 2012; Mirshamsi and Rafeeyan, 2015). It has been identified that the variation of the flow field is related to the structure of the PIT. In order to optimize the parameters of the PIT, the following three unknown quantitative parameters were taken into account along with their three levels: longitudinal initial velocity u, pressure head inclination angle θ, and PIT diameter d. External disturbance pressure P_d is added to take into account the marine pipeline. The three levels were assumed on the basis of the range of the main parameters in a previous study, as presented in Table 2 (Zhu et al., 2017). The objectives of the optimization scheme were to obtain the minimum drag coefficient and pressure coefficient.

Table 1
Parameters values.

Parameter	Value, mm	Parameter	Value, mm
l_1	25	d_1	33.5
l_2	20	d	37
l_3	25	d_3	37
l_4	20	D	50
θ	0°		

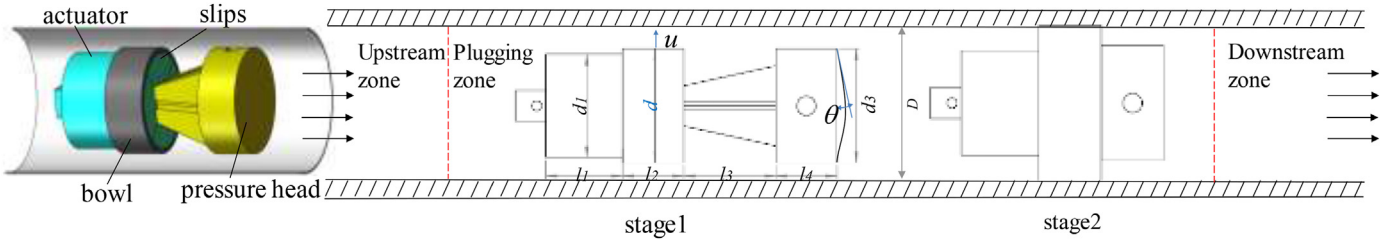

Fig. 1. Simplified dynamic PIT model.

Table 2
Four quantitative parameters and the three levels of the optimal model.

Level	Parameter			
	Longitudinal initial velocity, mm/s	Pressure head inclination angle, degree	Diameter, mm	Disturbance pressure, MPa
−1	0.1	0	36	1
0	0.2	22.5	38	3
1	0.3	45	40	5

The drag coefficient is widely used in the fields of aviation and automobile manufacturing as one of the important parameters in aerodynamics. By changing the external structure of an automobile and a spacecraft, the drag coefficient is reduced and the stability is improved (Khalighi et al., 2012). Therefore, it is of considerable significance to reduce the drag coefficient during operation in order to improve the stability by optimizing the external structure of the PIT. Pressure coefficient is also one of the commonly used parameters in the study of a flow field, which is essential for studying the phenomena of a flow around a blunt body and vortex shedding (Rastgou and Saedodin, 2013; Xiao et al., 2015). By reducing the pressure coefficient, we can simultaneously reduce the vortex phenomenon and the damage to the equipment caused by the vibration during the plugging process. Therefore, the drag coefficient C_d and the pressure coefficient C_p of the flow field in a natural gas pipeline were considered the development parameters (Yang and Wang, 2003). The following equations are recommended in fluid mechanics books and papers to be used as the drag coefficient and the pressure coefficient (Cóstola and Blocken et al., 2009; Guo et al., 2011).

$$C_d = \frac{F_d}{\frac{1}{2}\rho u^2 A_d} \tag{1}$$

$$C_p = \frac{\Delta P}{\frac{1}{2}\rho u^2} \tag{2}$$

where ΔP is the pressure difference between the upstream and the downstream of the PIT, F_d is the resistance of the object, ρ is the gas density, A_d is the cross-sectional area of the object perpendicular to the direction of flow motion, and μ is the mainstream velocity.

The surface structural optimization is an iterative process. In each iteration, the response surface of the objective function and the constraint function needs to be constructed. The objective function takes the complete quadratic function as the response surface function (Eq. (3)).

$$y(x) = \beta_0 + \sum_{i=1}^{n} \beta_i x_i + \sum_{i=1}^{n} \sum_{j=1, i<j}^{n} \beta_{ij} x_i x_j + \sum_{i=1}^{n} \beta_{ii} x_i^2 + \varepsilon \tag{3}$$

where x_i is an independent variable, β_0 is a constant term, β_i is a linear coefficient term, β_{ij} is an interaction term coefficient, β_{ii} is a quadratic coefficient of x_i, and ε is a random error. The random error in the simulation experiment is small and negligible, so in this design, $\varepsilon = 0$.

The experimental design method of the objective response surface adopts the CCD (Aksoy and Sagol, 2016). In a full factorial design, all the horizontal combinations of all the design variable components are required (Song et al., 2014). Obviously, this increases the experimental executives and the computational cost. However, CCD has wide applicability to the combination of the factors and the levels, and has the characteristics of rotatability, model robustness, and relatively few trials; furthermore, the regression equation obtained using this method has a good fitting property compared with the actual results. The distinguishing property of CCD from the other methods is the usage of axial points defined as the α value.

In the PIT structure optimization model, two response indices were defined, namely the drag coefficient (C_d) and the pressure coefficient (C_p). With the consideration of the linear terms, the quadratic term, the first-order interaction term, and the axial point α of the three quantitative parameters, the mathematical model of the reduced flow field vibration factors could be expressed as Eq. (4).

$$y = \beta_0 + \beta_1 x_1 + \beta_2 x_2 + \beta_3 x_3 + \beta_4 x_4 + \beta_{11} x_1^2 + \beta_{22} x_2^2 + \beta_{33} x_3^2 + \beta_{44} x_4^2 + \beta_{12} x_1 x_2 + \beta_{13} x_1 x_3 + \beta_{14} x_1 x_4 + \beta_{23} x_2 x_3 + \beta_{24} x_2 x_4 + \beta_{34} x_3 x_4 \tag{4}$$

For the purpose of obtaining the weighting values, 24 schemes were designed, and an optimal design was generated that included the 24 representatives shown in Table 3.

4. Results and discussion

4.1. Numerical results of CFD simulation

For pipeline flow, when the Reynolds number *Re* is greater than 12000, The flow in the tube is basically in a completely turbulent state. In this article, *Re*=133758.8. The parameters are shown in Table 4. According to the Reynolds similarity principle, the results are applicable to different pipelines with the same Reynolds number.

$$u_0 \geq \frac{Re\mu}{D\rho} \tag{5}$$

According to the existing PIT, the radial stroke of the plugging is 10–20 mm. Therefore, according to the simplified PIT model, a pipeline with a diameter of 50 mm was selected. According to the pre-simulation, the backflow and water hammer occurred within 500 mm downstream during the plugging process, so the pipeline length was chosen to be 1000 mm. The flow medium was simple-phase natural gas, and the center point of the PIT model coincided with the center point of the pipeline. The wall of the pipe and the PIT in contact with the fluid were defined as the no-slip wall boundary conditions.

In order to simulate the dynamic process of plugging, the actuator and slips were defined as the slip surfaces. Their motion velocities were set by writing a user-defined function. As the slips moved to the right, a complete dynamic plugging process was obtained. According to the PIT model size, the x-axis speed of the slip was set to 0.1 mm/s, and the y-axis speed was 0.26 mm/s. The x-axis speed of the actuator was set to 0.1 mm/s. The iteration was stopped when the plugging ratio reached 98%, because the CFD software could not continue to run when the flow was 0.

After setting the boundary conditions and selecting the models that conformed to the physical properties, the mass energy and momentum equations were solved in a 2D space limited by the domain boundaries. The previous research has shown that before

Table 3
CCD schemes and results of two response indices.

Scheme	Longitudinal initial velocity, mm/s	Pressure head inclination angle, degree	Diameter, mm	Disturbance pressure, MPa	Drag coefficient	Pressure coefficient
1	0.1	0.0	40	1	4.950	−5.446
2	0.2	22.5	40	3	3.304	−6.211
3	0.3	45.0	36	1	0.361	−2.845
4	0.2	45.0	38	3	1.809	−4.380
5	0.2	22.5	36	3	1.848	−3.432
6	0.3	22.5	38	3	3.376	−4.424
7	0.2	0.0	38	3	3.507	−4.418
8	0.1	0.0	40	5	5.692	−6.263
9	0.1	45.0	40	5	3.063	−6.600
10	0.1	45.0	40	1	2.663	−5.739
11	0.1	22.5	38	3	2.829	−4.441
12	0.1	45.0	36	1	0.553	−2.613
13	0.2	22.5	38	5	3.094	−4.651
14	0.3	0.0	40	1	4.262	−5.735
15	0.3	45.0	40	5	3.211	−5.408
16	0.3	45.0	36	5	0.415	−3.272
17	0.3	0.0	40	5	4.902	−6.595
18	0.1	0.0	36	5	2.326	−3.258
19	0.3	0.0	36	1	2.442	−3.149
20	0.3	45.0	40	1	2.793	−4.702
21	0.1	45.0	36	5	0.636	−3.005
22	0.2	22.5	38	1	2.691	−4.045
23	0.1	0.0	36	1	2.023	−2.833
24	0.3	0.0	36	5	2.809	−3.622

Table 4
Numerical simulation parameters.

Parameter	Symbol	Value	Unit
Density of natural gas	ρ	0.717	kg/m^3
Dynamic viscosity of natural gas	μ	1.7894×10^{-5}	Pa·s
Initial pressure difference	ΔP	0.1	MPa
Inlet flow	Q_0	66.76	m^3/h
Turbulence intensity	T_i	2.8–4.45	%
Hydraulic diameter	H_D	0.05	m

the plugging ratio reached 80%, the length of the backflow area was in positive proportion to the plugging ratio (Zhao and Hu, 2017). The pressure in the downstream zone increased with an increase in the plugging ratio. The upstream zone was a low-pressure backflow area and generated a pressure pulse. With an increase in the plugging ratio, the area was diffused continuously, and the pulsation intensity was strengthened accordingly, which was harmful to the safety of the pipe and the PIT.

As the plugging progresses, the distance between slips and the pipeline decreased and the rate of change of fluid flow rate was greater, so the outwall of slips was selected as the research object. Fig. 2 shows the pressure values under different plugging conditions of the outwall of slip. The pressure was relatively low near the axis. The pressure values at 0–14 mm first increased and then decreased. The pressure values increased exponentially after 0.014 m. The first half was the low-pressure backflow area, and the second half, the high-pressure danger area. When the plugging ratio was between 20%–40% and 80%–99%, the pressure changed considerably and the intermediate process changed slowly. The pressure difference between the upstream and the downstream of the PIT (ΔP) and the resistance of the object (F_d) were obtained by the CFD simulations. The drag coefficient (C_d) and the pressure coefficient (C_p) were calculated from Eq. (1) and Eq. (2) which are listed in Table 3. When the plugging operation started and ended, the flow field vibrated considerably, which was a dangerous time. Fig. 3 shows the dynamic pressure change curve of schemes 8–12 (Table 3) on the pipeline. Schemes 12 had the smallest sum of pressure, i.e.,$\min|C_d| + |C_p|$. Schemes 8 and 12 had the least fluctuation in the peak values, i.e., $\min|C_d|$. Therefore, changing the surface structure could reduce the pulsation and make the plugging process safer.

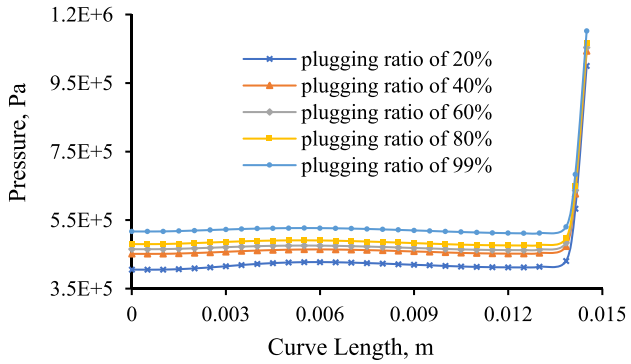

Fig. 2. Total pressure values under different plugging conditions on outwall of slip.

4.2. Structural optimization results

According to the determined design, 24 experiments for the four parameters were carried out. The drag coefficient and the pressure

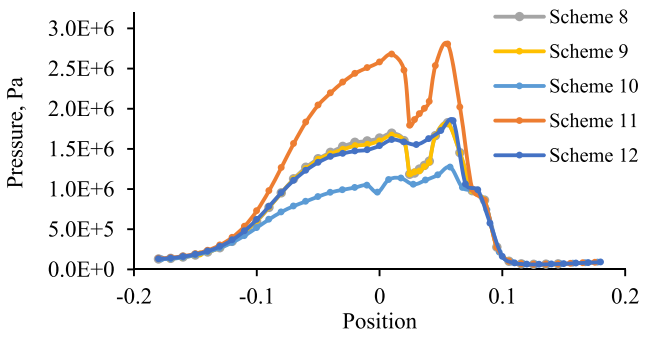

Fig. 3. Dynamic pressure change curves of five schemes applied to a pipeline.

coefficient obtained from these experiments were given along with the design matrix. As shown in Table 3, the change in the drag coefficient was between 0.36 and 5.69; the change in the pressure coefficient was between −2.61 and −6.60. Therefore, the surface structure of the PIT had a more significant effect on the drag coefficient. The results of the experiments were subjected to a variance analysis for both the response variables, and regression models were formed. The relationship between the response and the independent variables was demonstrated using a response surface plot.

4.2.1. Influences of structural optimization model on drag coefficient

According to the results presented in Table 3, the equation of the drag coefficient as a function of different variables was obtained as follows:

$$\begin{aligned} C_d = & -117.38 + 9.46 \times u - 0.94 \times 10^{-3} \times \theta + 5.76 \times d \\ & -0.77 \times P_d + 0.01 \times u \times \theta - 0.53 \times u \times d - 0.02 \times u \times P_d \\ & -0.61 \times 10^{-3} \times \theta \times d - 1.5 \times 10^{-3} \times \theta \times P_d + 0.02 \times d \times P_d \\ & +25.74 \times u^2 - 0.37 \times 10^{-3} \times \theta^2 - 0.07 \times d^2 + 0.01 \times P_d^2 \end{aligned} \quad (6)$$

Table 5 presents the ANOVA results of this evaluation model. The F-value of 21.91 implied that the model was significant. There was only a 0.01% chance that a large F-value could occur because of noise. A P-value of less than 0.0500 indicated that the model terms were significant.

In this model, the P-values for the pressure head inclination angle and the diameter were less than 0.001; thus, they were significant for the model. The magnitude of the influence of the four parameters on the model was the pressure head inclination angle, diameter, disturbance pressure and longitudinal initial velocity. The correlation factor of 0.9715 showed a good agreement between the fitting correlation and the data points. "Adeq Precision" measured the signal-to-noise ratio. This case ratio of 16.626 indicated an adequate signal. This model could be used to navigate the design space.

In order to emphasize the influence of different variables on the drag coefficient, the weighted results were analyzed. Two quantitative parameters, namely θ and d, which fell to the right of "95% confidential level" line were considered the significant variables. The longitudinal initial velocity made marginal contributions to the drag coefficient. In order to attest the surface structural optimization model of the drag coefficient, the calculated results using the surface structural optimization model were compared with those obtained by the CFD simulation runs for 24 CCD schemes, as shown in Fig. 4. All of the data were distributed near a line that had a (0,0) point and a slope of 1, and did not exceed the specified range. Therefore, the surface structural optimization model of the drag coefficient factor was proven to be valid and reasonable. Fig. 5 shows the normal probability of the residuals, which indicated whether the residuals followed a normal distribution. The studentized residual of the output value was the x-axis, and its percentage was the y-axis. The drag coefficient was irregularly distributed around the straight line and was approximated as a straight line. Therefore, it could be approximated as a normal distribution curve. Fig. 6 illustrates the relationship between the first-order parameters. When the diameter and disturbance pressure were constant, the pressure head inclination angle first decreased and then increased as the longitudinal initial velocity increased. When the longitudinal initial velocity was around 0.2 mm/s, the pressure head inclination angle was minimum. When the pressure head inclination angle and disturbance pressure were constant, the diameter first increased and then decreased as the longitudinal initial velocity increased. When the longitudinal initial velocity was around 0.2 mm/s, the diameter was maximum. When the pressure head inclination angle and diameter were constant, the disturbance

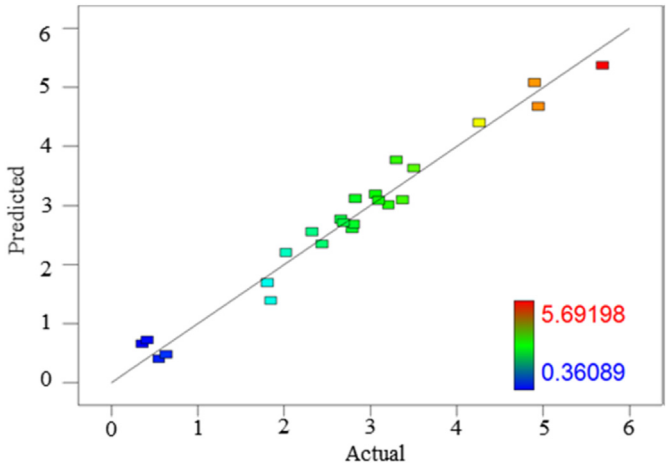

Fig. 4. Comparison between calculated results and simulation results of drag coefficient.

Table 5
ANOVA of structural optimization model of drag coefficient.

Source	Sum of squares	df	Mean square	F value	P value Prob > F	R^2	Adeq precision
Model	43.80	14	3.13	21.91	<0.0001	0.9715	16.626
u	1.49×10^{-3}	1	1.49×10^{-3}	0.010	0.9210		
θ	16.84	1	16.84	117.95	<0.0001		
d	25.50	1	25.50	178.63	<0.0001		
P_d	0.65	1	0.65	4.53	0.0623		
$u \times \theta$	0.012	1	0.012	0.084	0.7779		
$u \times d$	0.18	1	0.18	1.25	0.2922		
$u \times P_d$	0.15×10^{-3}	1	0.15×10^{-3}	1.08×10^{-3}	0.9746		
$\theta \times d$	0.012	1	0.012	0.085	0.7771		
$\theta \times P_d$	0.075	1	0.075	0.53	0.4867		
$d \times P_d$	0.12	1	0.12	0.85	0.3807		
u^2	0.17	1	0.17	1.17	0.3070		
θ^2	0.089	1	0.089	0.62	0.4512		
d^2	0.18	1	0.18	1.28	0.2869		
P_d^2	5.70×10^{-3}	1	5.70×10^{-3}	0.040	0.8461		
Residual	1.29	9	0.14				
Cor total	45.09	23					

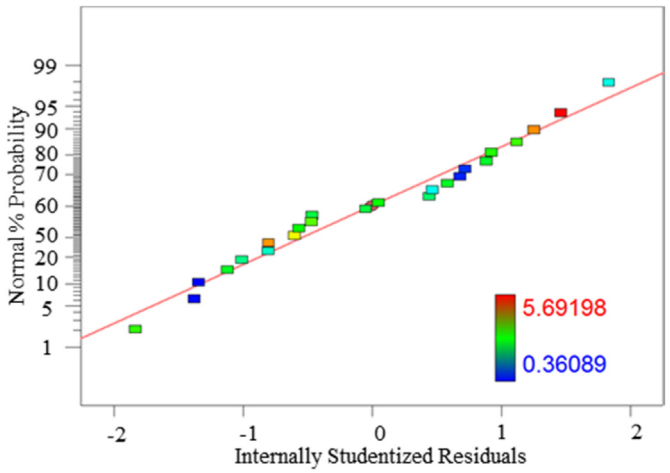

Fig. 5. Residuals' normal probability of drag coefficient.

pressure first increased and then decreased as the longitudinal initial velocity increased. When the longitudinal initial velocity was around 0.2 mm/s, the disturbance pressure was maximum. The longitudinal initial velocity had the greatest influence on the disturbance pressure.

The contour line density was the highest, as shown in Fig. 6**f**, so the correlation between the disturbance pressure and the diameter was more significant. The correlation between the longitudinal initial velocity and the disturbance pressure was the worst. This result was consistent with the ANOVA results.

4.2.2. Influences of structural optimization model on pressure coefficient

Applying the same methodology of the surface structural optimization model, we obtained the correlation of the pressure coefficient as a function of different variables on the basis of the results presented in Table 3 as follows:

$$\begin{aligned} C_p = &-81.60 - 38.26 \times u - 0.05 \times \theta + 4.94 \times d + 0.49 \times P_d \\ &+0.08 \times u \times \theta + 0.87 \times u \times d + 9.33 \times 10^{-3} \times u \times P_d \\ &+0.64 \times 10^{-3} \times \theta \times d + 0.26 \times 10^{-3} \times \theta \times P_d - 0.02 \times d \times P_d \\ &+8.68 \times u^2 + 0.24 \times 10^{-3} \times \theta^2 - 0.08 \times d^2 + 0.04 \times P_d^2 \end{aligned} \tag{7}$$

Equation (7) represents the surface structural optimization model of the pressure coefficient. According to the ANOVA results of this evaluation model presented in Table 6, the F-value was 48.61 that the model was significant. The P-value was smaller than 0.0001, which implied that the model was even reliable at the 99% confidential level. The correlation factor of 0.9860 showed a good agreement between the fitting correlation and the data points. This case ratio of 20.443 indicated an adequate signal. Therefore, the model could be used to navigate the design space.

In order to emphasize the influence of different variables on the pressure coefficient, the weighted results were analyzed. With regard to the linear terms of the three quantitative parameters given in Table 6, the most influential parameter was diameter d, disturbance pressure P_d, pressure head inclination angle θ, and longitudinal initial velocity u, with a decreasing significance to the surface structural optimization model of the pressure coefficient.

With the purpose of verifying the surface structural optimization model of the pressure coefficient, Fig. 7 compared the calculated results and the simulation results of the pressure coefficient. The results were in perfect agreement with the CFD simulation results. Fig. 8 shown that the model presented a quadratic regression distribution. The surface structural optimization model of the pressure coefficient was proven to be valid and reasonable. As each factor increased, the longitudinal initial velocity first increased and then decreased, the pressure head inclination angle first increased and then decreased, and the diameter increased. When the longitudinal initial velocity was between 0.15 and 0.35 and the pressure head inclination angle was between 0.38 and 18.38, the diameter obtained the optimum value. The optimal values of the longitudinal initial velocity and the pressure head inclination angle could not be obtained intuitively and required further optimization.

4.3. Optimization based on modified PSO

At the optimization stage, the RSM could not be used to predict the optimal value of the response variable from the regression model. The PSO algorithm was used because of its advantages of swarm intelligence, inherent parallelism, simple iterative format, and rapid convergence (Gordan et al., 2016). Compared with the modified GA, PSO only needs the original mathematical operators in the iterative process. It does not need genetic operators such as reproduction, crossing, and mutation. Therefore, the calculation process of PSO is relatively simple and easy to implement. Meanwhile, an objective function is directly used as fitness function to guide the search in PSO, making it easy to handle a non-linear optimization problem (Yu et al., 2004). Therefore, the PSO algorithm was selected in this study.

4.3.1. Optimization design

The PSO algorithm found the optimal solution through repeated iterations. In each iteration, the particle was updated by tracking two extremum values. The two extremum values were the individual optimal solution and the global optimal solution, respectively. During the optimization process, the velocity and the position of the particle were updated according to Eqs. (8) and (9), respectively.

$$v_{i,j}(t+1) = v_{i,j}(t) + c_1 r_1 \left[p_{i,j} - x_{i,j}(t)\right] + c_2 r_2 \left[p_{g,j} - x_{i,j}(t)\right] \tag{8}$$

$$x_{i,j}(t+1) = x_{i,j}(t) + v_{i,j}(t+1) \tag{9}$$

where i is the current particle, j is the current dimensional space, c_1 and c_2 are the learning factors, and r_1 and r_2 are two random numbers at [0, 1]. If $v_{i,j} > v_{max}$, $v_{i,j} = v_{max}$; if $v_{i,j} < -v_{max}$, $v_{i,j} = -v_{max}$.

From the above discussion, the minimization of the drag coefficient C_d and the pressure coefficient C_p was considered to reduce the effects and the differences in the two directions to achieve a steady control environment. The objective function could be expressed as Eq. (10). As the two target values could not be minimized at the same time, the two target values were weighted. We assumed that the two target values had the same influence on the field, $\lambda = 0.5$. Because the disturbance pressure was uncontrollable, it could not be optimized. The constraints function could be expressed as Eq. (11).

$$\min|C| = \lambda|C_d| + (1-\lambda)|C_p| \tag{10}$$

$$s.t. \begin{cases} 0.1 \le u \le 0.3 \\ 0 \le \theta \le 45 \\ 36 \le d \le 40 \end{cases} \tag{11}$$

When the basic PSO algorithm was applied, the resulting error was large, because the optimization model fell into local

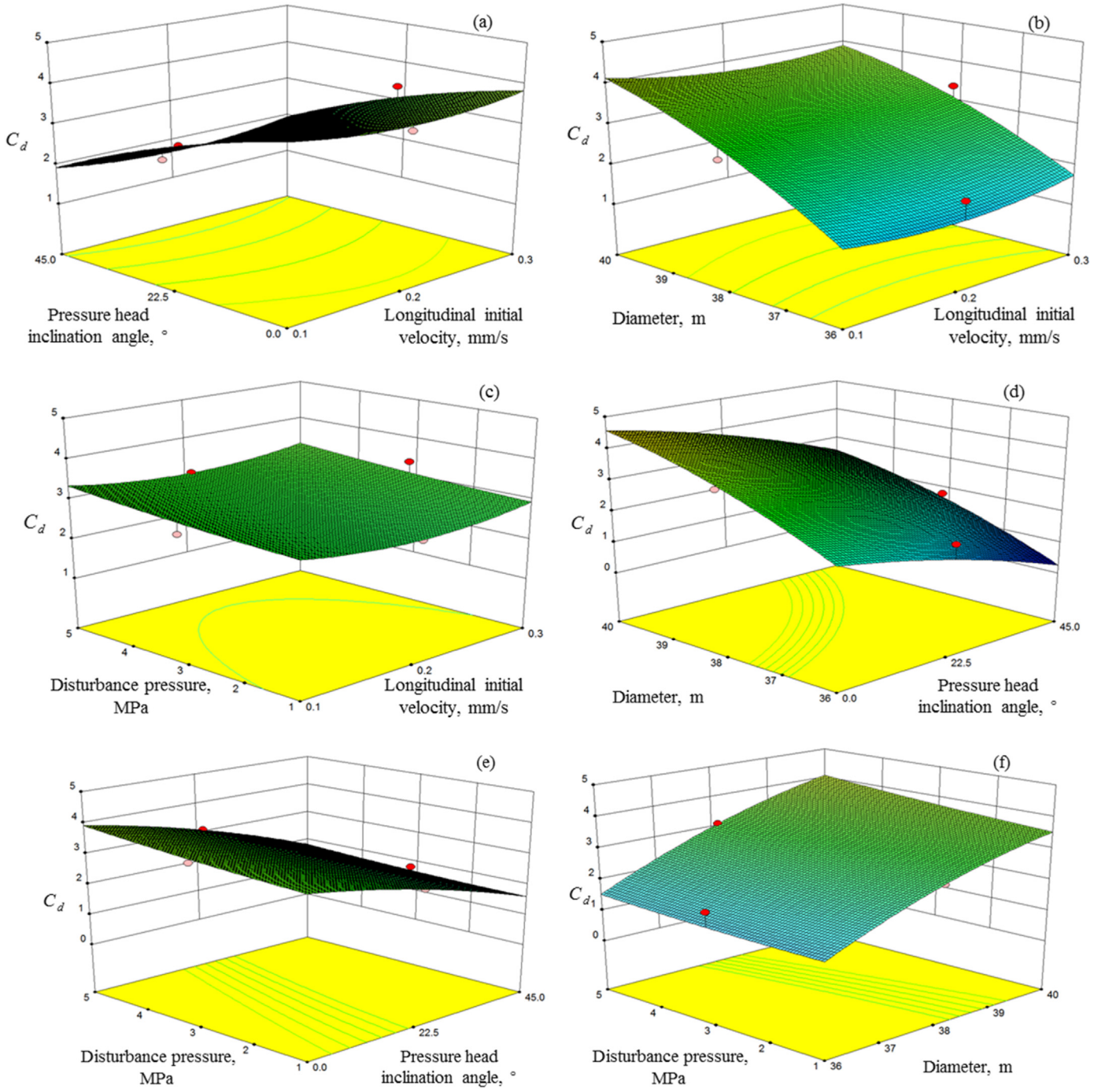

Fig. 6. Relationship between the first-order parameters: **a** relationship between longitudinal initial velocity and pressure head inclination angle, **b** relationship between longitudinal initial velocity and diameter, **c** relationship between disturbance pressure and longitudinal initial velocity **d** relationship between pressure head inclination angle and diameter, **e** relationship between disturbance pressure and pressure head inclination angle, **f** relationship between disturbance pressure and diameter.

optimization. Therefore, the PSO algorithm was improved. Equation (8) was modified, and the inertia weighting factor ω was introduced.

$$v_{i,j}(t+1) = \omega v_{i,j}(t) + c_1 r_1 \left[p_{i,j} - x_{i,j}(t)\right] + c_2 r_2 \left[p_{g,j} - x_{i,j}(t)\right] \quad (12)$$

$$\omega = \omega_{\max} - \frac{t \times (\omega_{\max} - \omega_{\min})}{\omega_{\max}} \quad (13)$$

where ω_1, ω_2 represent the maximum and the minimum values of ω, respectively; t represents the current iteration step, and $t_{\max}$ represents the maximum number of iteration steps. Because the larger weight factor was advantageous to jump out of the local minimum point, it facilitated the global search. The small inertia factor was helpful for an accurate local search of the current search area. Therefore, the weight of the linear change was adopted to reduce the weight of the inertia from the maximum to the minimum.

In this case, the initial seed was selected as 24. The maximum

Table 6
ANOVA of structural optimization model of pressure coefficient.

Source	Sum of squares	df	Mean square	F value	P value Prob > F	R^2	Adeq precision
Model	37.49	14	2.68	48.61	<0.0001	0.9869	20.443
u	0.011	1	0.011	0.20	0.6661		
θ	0.42	1	0.42	7.65	0.0219		
d	33.81	1	33.81	613.82	<0.0001		
P_d	1.72	1	1.72	31.25	0.0003		
$u \times \theta$	0.57	1	0.57	10.42	0.0104		
$u \times d$	0.49	1	0.49	8.82	0.0157		
$u \times P_d$	0.06×10^{-3}	1	0.06×10^{-3}	1.01×10^{-3}	0.9753		
$\theta \times d$	0.013	1	0.013	0.24	0.6349		
$\theta \times P_d$	2.24×10^{-3}	1	2.24×10^{-3}	0.041	0.8445		
$d \times P_d$	0.15	1	0.15	2.65	0.1382		
u^2	0.019	1	0.019	0.35	0.5709		
θ^2	0.037	1	0.037	0.67	0.4357		
d^2	0.23	1	0.23	4.19	0.0710		
P_d^2	0.074	1	0.074	1.34	0.2760		
Residual	0.50	9	0.055				
Cor total	37.98	23					

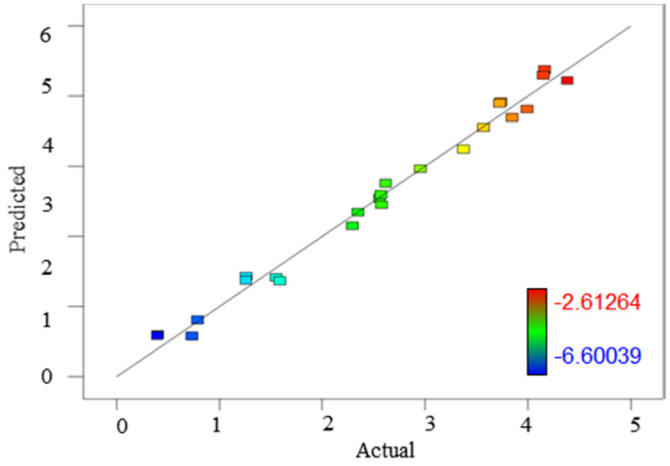

Fig. 7. Comparison between calculated results and simulation results of pressure coefficient.

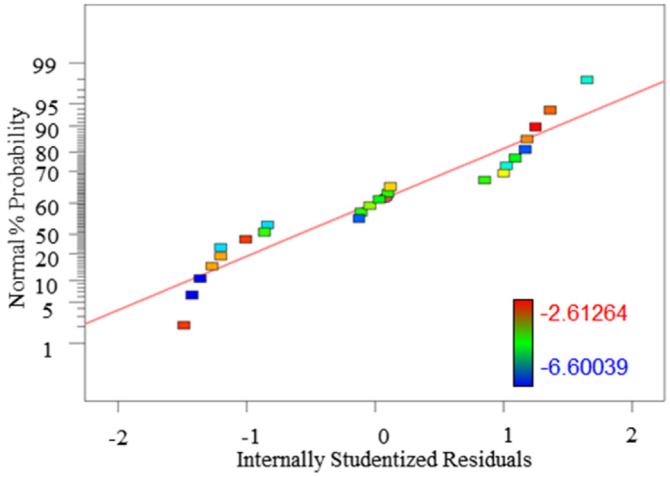

Fig. 8. Residuals' normal probability of pressure coefficient.

number of iterations was 2000. The weighted values at the initial time and convergence time were 0.9 and 0.4, respectively. When the optimal value of the corresponding population was less than $1e^{-25}$ in two consecutive iterations, the algorithm stopped.

The surface structural optimization model of the drag coefficient and the pressure coefficient models were optimized by PSO. The drag coefficient and the pressure coefficient were each weighted by 0.5, and the obtained optimization parameter was called "Model 1", as shown in Fig. 9. The minimum point (0.164593, 45, 36) was obtained, and the minimum value was 1.52126. When the number of iterative steps was less than 50, it was close to the minimum value. So it had a significant advantage in terms of the speed of convergence. The drag coefficient was close to the theoretical minimum in aerodynamics, so the accuracy of the optimization was very successful. However, the maximum number of iterations was difficult to predict, which affected the adjustment function of the algorithm.

The unoptimized parameter was called "Model 0", which was (0.1, 0, 37). In order to verify the effectiveness of PSO, modified GA was applied to the optimization under the same objective function (Eq. (10)) and constraints function (Eq. (11)). The selected population quantity was 20, the length of each population was 20, the generation gap was 0.9, and the optimized result was called "Model 2". Compared with the results obtained by different optimization methods, the improved PSO had the best effect, followed by the modified GA, as shown in Fig. 10. The drag coefficient was greatly affected by the surface structural parameters of the PIT. After the modified GA optimization, the vibration of the PIT model system decreased by 47.95%. After PSO, the vibration of the PIT model system was reduced by 49.56%. Therefore, PSO was more accurate and effective in optimizing the structure of the PIT.

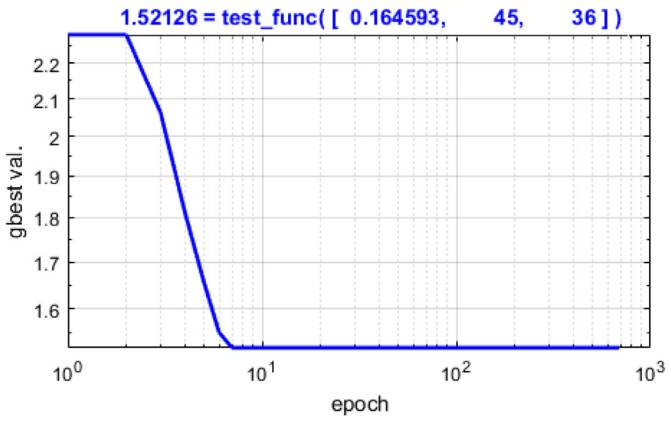

Fig. 9. Structural model optimization results.

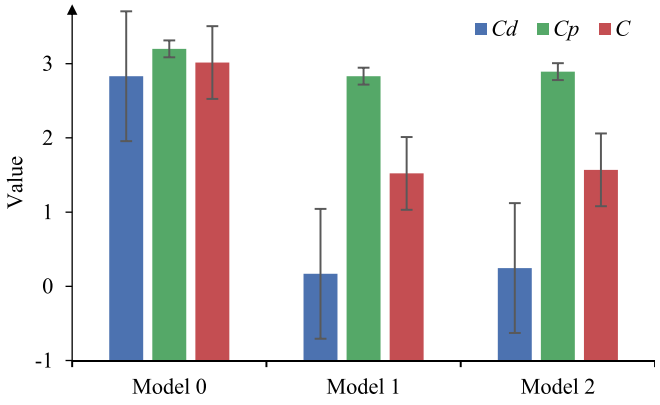

Fig. 10. Comparison of the results of different optimization methods.

4.3.2. Experimental device and experimental validation

In order to verify the simulation results, design the experimental device shown in Fig. 11. It mainly includes hydraulic pump, pressure reducing valve, flow meter, pressure sensor and data acquisition system. Among them, the flow meter was used to measure the average flow rate inside the pipe. The pressure signal of the test pipe wall was converted into a voltage signal through the pressure sensor. The pressure data were collected by using the data acquisition card and the pre-programmed LABVIEW data acquisition program. Finally, the real-time change value of the wall pressure was obtained.

According to previous research, as the plugging ratio increases, the flow field changes more drastically. Therefore, the designed pressure observation points are non-uniformly distributed. The closer to the complete blockage, the denser the observation points. In this experiment, the pressure measurement was carried out for seven points near the plugging point, i.e., A–G in Fig. 11, where A, B, and C were stage 1 and D was stage 2. E, F, and G were the pressure relief stages.

The experiment measured the flow field pressure of "Model 0", "Model 1" and "Model 2". The real-time variation of the wall pressure signal was collected in the experiment, and the time domain signals were converted into frequency domain signals by signal transformation for the frequency domain analysis. The time domain diagram in Fig. 12 shows that the pressure changes at each measurement point were relatively large but basically fluctuated around the mean pressure. Comparing the time domain graphs of different models, we found that the pressure pulse of "Model 1" was the smallest. Comparing the time domain diagram from point A to point G of the same model, we found that the pressure pulse at point D was the largest, and the pressure pulses at the left and the right points were sequentially decreased.

According to the frequency domain diagram of pressure pulsation, the pressure pulsation frequencies of the seven measurement points (point A–point G) were mainly concentrated at 6.35 Hz, 31.77 Hz, 73.07 Hz, 101.67 Hz, and 158.86 Hz. The pressure pulsation amplitude was the largest when the frequency was 6.35 Hz; therefore, 6.35 Hz could be considered the basic frequency of the pressure pulsation of the pipe wall. Fig. 13 shows the frequency of the highest amplitude of each measurement point at the plugging completion. The figure shows that the frequency of the highest amplitude at the detection points G and A was relatively small and was less affected by the model structure. The pressure variation of the middle five monitoring points was considerably affected by the model structure, and the pressure fluctuation was significant. A comparison of the three surface structural models revealed that the frequency of the highest amplitude of "Model 1" was the smallest. Compare Model 1 with Zhao and Hu (2017)'s model, as shown in Fig. 14. The total force in the *x* direction of Model 1 was reduced by 11.14%. The total force in the *y* direction of Model 1 was reduced by 36.63%. Therefore, it was proven that the vibration of the flow field was smaller when "Model 1" was used for plugging, and the process of plugging was more stable and safer.

5. Conclusions

The main purpose of this paper is to improve our understanding of influence on the flow field vibration during the plugging process by the external structure of the PIT through numerical analysis and experiments. The corresponding drag coefficient and pressure coefficient were obtained through the dynamic finite element model. A visual experimental rig was developed to measure and observe the vibration of the flow field. Finally, a mathematical model of flow field vibration and PIT structure was obtained. Each parameter in the mathematical model was optimized and the PIT structure with the minimum flow field vibration was obtained through the improved PSO.

The effects of the longitudinal initial velocity, pressure head inclination angle, and diameter of the PIT on the flow field vibration and the results were compared with the simulation results conducted before. The research results indicated that the increase of the three parameters can cause the flow field vibration to decrease first and then increase. The longitudinal initial velocity of the PIT has the greatest influence on the flow field vibration, followed by the PIT diameter and then the PIT pressure head inclination angle. The improved model can reduce the total force of the PIT in the x direction by 11.14% and the total force in the y direction by 36.63%. The vibration of the flow field is reduced by 49.56%. This study can provide a reference for safe and durable pipeline blockage.

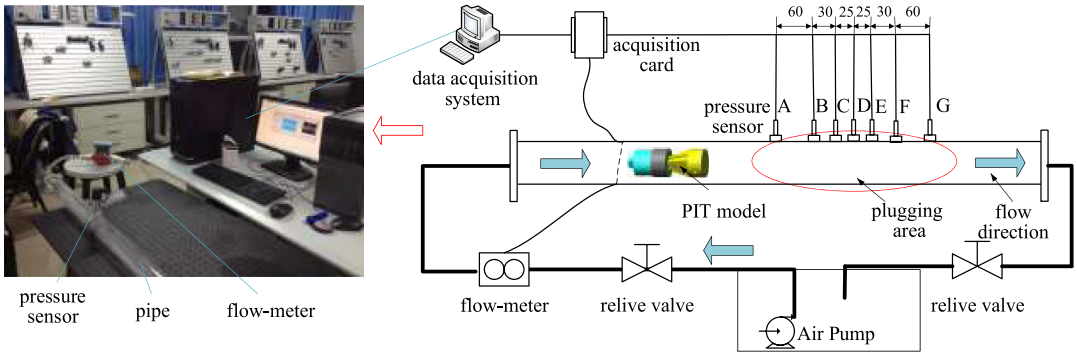

Fig. 11. Experimental device.

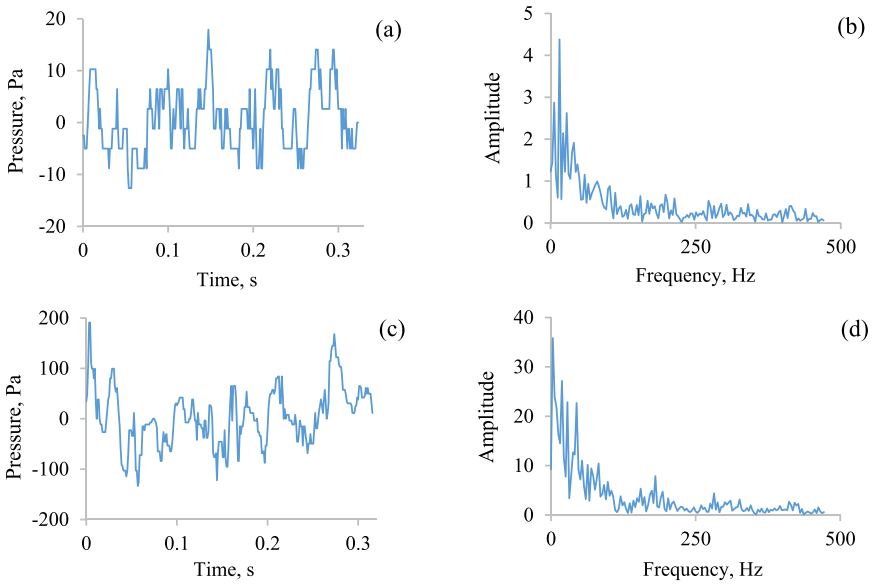

Fig. 12. Time domain and frequency domain graphs of detected points A and D at the plugging completion of "Model 1": a time domain graph of point A, b frequency domain graph of point A, c time domain graph of point D, and d frequency domain graph of point D.

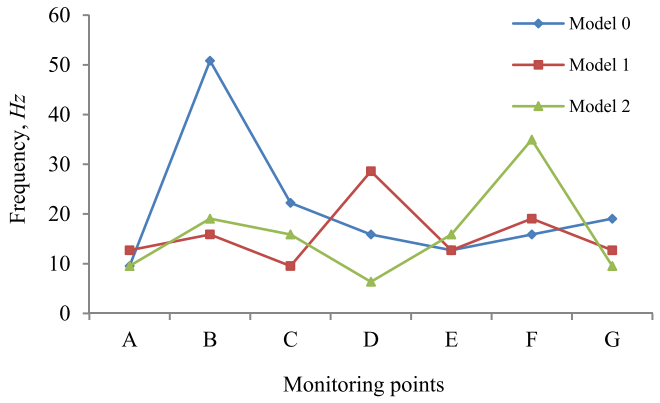

Fig. 13. Frequency of the highest amplitude at the plugging completion.

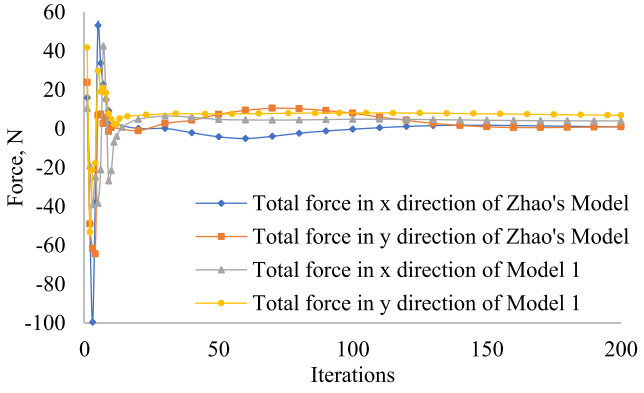

Fig. 14. Comparison of the total force obtained by Zhao and Hu (2017) with a simulation.

Acknowledgments

This work was financially supported by the National Natural Science Foundation of China (Grant No. 51575528).

References

Aksoy, D.O., Sagol, E., 2016. Application of central composite design method to coal flotation: modelling, optimization and verification. Fuel 183, 609–616. https://doi.org/10.1016/j.fuel.2016.06.111.

Cóstola, D., Blocken, B., et al., 2009. Overview of pressure coefficient data in building energy simulation and airflow network programs. Build. Environ. 44 (10), 2027–2036. https://doi.org/10.1016/j.buildenv.2009.02.006.

Dolejal, L., Tveit, E., 2001. The Smart plug remotely controlled pipeline isolation system. In: Offshore mediterranean conference and exhibition. Ravenna, Italy, Offshore Mediterranean Conference, 14.

Edd Tveit, J.A., 2000. In: Remote Controlled (Tether-Less) High Pressure Isolation System. SPE Asia Pacific Oil and Gas Conference and Exhibition. https://doi.org/10.2118/64513-MS. Brisbane, Australia.

Gordan, B., Armaghani, D.J., et al., 2016. Prediction of seismic slope stability through combination of particle swarm optimization and neural network. Eng. Comput. 32 (1), 1–13. https://doi.org/10.1007/s00366-015-0400-7.

Guo, Xiaohui, Lin, Jianzhong, Nie, Deming, 2011. New formula for drag coefficient of cylindrical particles. Particuology 9 (2), 114–120. https://doi.org/10.1016/j.partic.2010.07.027.

Khalighi, B., Jindal, S., et al., 2012. Aerodynamic flow around a sport utility vehicle—computational and experimental investigation. J. Wind Eng. Ind. Aerod. 107–108, 140–148. https://doi.org/10.1016/j.jweia.2012.04.009.

Liang, Z., He, H., et al., 2017. Speed simulation of bypass hole PIG with a brake unit in liquid pipe. J. Nat. Gas Sci. Eng. 42, 40–47. https://doi.org/10.1016/j.jngse.2017.03.011.

Lie, R.G., Muangsuankwan, N., 2015. Remote-controlled plugging technology minimizes platform downtime: valve replacement through SmartPlug® isolation. In: ASME 2015 India International Oil and Gas Pipeline Conference. American Society of Mechanical Engineers. https://doi.org/10.1115/IOGPC2015-7910.

Mirshamsi, M., Rafeeyan, M., 2015. Dynamic analysis and simulation of long pig in gas pipeline. J. Nat. Gas Sci. Eng. 23, 294–303. https://doi.org/10.1016/j.jngse.2015.02.004.

Rastgou, H., Saedodin, S., 2013. Numerical simulation of an axisymmetric separated and reattached flow over a longitudinal blunt circular cylinder. J. Fluid Struct. 42, 13–24. https://doi.org/10.1016/j.jfluidstructs, 2013.05.006.

Solghar, A.A., Davoudian, M., 2012. Analysis of transient PIG motion in natural gas pipeline. Mech. Indus. 13 (5), 293–300. https://doi.org/10.1051/meca/2012039.

Song, C., Kwon, K., et al., 2014. Optimum design of the internal flushing channel of a

drill bit using RSM and CFD simulation. Int. J. Precis. Eng. Manuf. 15 (6), 1041–1050. https://doi.org/10.1007/s12541-014-0434-6.
Song, Z., Li, Z., et al., 2014. D-optimal design for Rapid Assessment Model of CO_2 flooding in high water cut oil reservoirs. J. Nat. Gas Sci. Eng. 21, 764–771. https://doi.org/10.1016/j. jngse. 2014.10.005.
Tveit, E., Aleksandersen, J., 2000. Remote controlled (Tether-Less) high pressure isolation system. In: SPE Asia Pacific Oil and Gas Conference and Exhibition, vol. 8. Society of Petroleum Engineers, Brisbane, Australia. https://doi.org/10.2118/64513-MS.
Xiao, H., Xu, Z., et al., 2015. Experimental research on a hypersonic configuration with blunt forebody edges. Int. J. Precis. Eng. Manuf. 16 (10), 2115–2120. https://doi.org/10.1007/s12541-015-0273-0.
Yang, N., Wang, W., et al., 2003. CFD simulation of concurrent-up gas–solid flow in circulating fluidized beds with structure-dependent drag coefficient. Chem. Eng. J. 96 (1–3), 71–80. https://doi.org/10.1016/j.cej.2003.08.006.
Yu, X., Xiong, X., et al., 2004. A PSO-based approach to optimal capacitor placement with harmonic distortion consideration. Elec. Power Syst. Res. 71 (1), 27–33. https://doi.org/10.1016/j.epsr.2004.01.002.
Zhang, H., Zhang, S., et al., 2015. Chatter vibration phenomenon of pipeline inspection gauges (PIGs) in natural gas pipeline. J. Nat. Gas Sci. Eng. 27, 1129–1140. https://doi.org/10.1016/j.jngse, 2015.09.054.
Zhao, H., Hu, H., 2017. Optimal design of a pipe isolation plugging tool using a computational fluid dynamics simulation with response surface methodology and a modified genetic algorithm. Adv. Mech. Eng. 9 (10). https://doi.org/10.1177/1687814017715563, 1687814017715563.
Zhao, H., Zhao, Y., et al., 2016. Interactions between the fluid and an isolation tool in a pipe: laboratory experiments and numerical simulation. Petrol. Sci. 13 (4), 746–759. CNKI:SUN:SYKX.0.2016-04-010.
Zhu, X., Zhang, S., et al., 2015. Numerical simulation of contact force on bi-directional pig in gas pipeline: at the early stage of pigging. J. Nat. Gas Sci. Eng. 23, 127–138. https://doi.org/10.1016/j.jngse, 2015.01.034.
Zhu, X., Wang, W., et al., 2017. Experimental research on the frictional resistance of fluid-driven pipeline robot with small size in gas pipeline. Tribol. Lett. 65 (2). https://doi.org/10.1007/s11249-017-0830-z.